Ocean and Coastal Research

ORIGINAL ARTICLES

http://doi.org/10.1590/2675-2824071.220103jat
ISSN 2675-2824

Influence of Tokar Gap wind jet on latent heat flux of Central Red Sea: empirical orthogonal function approach

Jamaan A. Turki, Abdullah M. Al-Subh, Fawaz Madah

King Abdul-Aziz University, Faculty of Marine Sciences, Department of Marine Physics, Jeddah, Saudi Arabia.

* Corresponding author: jjamaanturki@stu.kau.edu.sa

ABSTRACT

The aim of this study was to investigate the main factors that influence the latent heat fluxes (LHF) in the Tokar Gap in the central part of the Red Sea. From 2000 to 2020, ERA5 reanalysis data on summer months of the Central Red Sea were used to match the time when the Tokar Wind Jet appeared. The diurnal variability of the Tokar Gap peaks in the early morning. The time series data of the wind speed showed that the Tokar Wind Jet appeared from July to August. The empirical orthogonal functions (EOF) analysis method was used to determine the modes of LHF variabilities. The sum of the first two modes of variability explained ~ 90.8% of the total variance. The first mode explained 80.8%, whereas the second mode represented approximately 9.9%. To examine the contribution of sea surface temperature (SST) and wind speed to the first two EOF principal components, the correlation coefficient and determination coefficient were applied. The results showed that SST had a CC of 0.90 and a DC of 81.99%, whereas wind speed showed a CC of 0.35 and a DC of 12.80%. These results may be explained by the strong link between SST and the specific humidity differences of saturation and actual vapor pressure. Partial correlation results indicate that there is an indirect relation between wind and LHF. In this study SST was the dominant factor, influencing LHF variability in the study area.

Keywords: ERA5 validation, EOF principal components, Partial correlation, Correlation coefficient, Determination coefficient.

INTRODUCTION

The Red Sea is a tropical semi-enclosed water basin located between the Arabian Peninsula and Africa. It stretches south-east to north-west between 12°N and 30°N latitude and 32°E and 44°E longitude (Figure 1). The Red Sea measures about 2,000 km in length, 280 km in width, and 500 m in depth (Morcos, 1970).

The Red Sea wind system is characterized by seasonal and regional variations. Due to the topographic features surrounding the Red Sea basin, the wind is driven along the basin (Patzert, 1974). The dominant wind pattern is the north-westerly winds from the Mediterranean weather system. However, during winter (November to April), the monsoon system from the Indian Ocean generates a prevailing south-westerly wind observed in the northern Indian Ocean, which blows from southwest in the southern part of the Red Sea (south of 20°N). In addition, these two dominant winds converge around 19°N. Moreover, there are two dominant cross-axis winds in the Red Sea basin, namely the Tokar Wind Jet and the north-westward jets from the east of the Red Sea (Langodan et al., 2017).

Mountain chains of various altitudes cover almost the entirety of both coastlines of the Red Sea.

Submitted: 28-April-2023
Approved: 04-May-2023

Editor: Cesar Rocha

These differences in height can drive winds to blow from high-pressure to low-pressure areas, which, in turn, generate wind gaps (Jiang et al., 2009; Langodan et al., 2017; Pratt et al., 2020). Wind gaps were first studied at the Strait of Juan de Fuca by Reed (1931) as cited in Alawad et al. (2020). Since then, wind gaps have been examined in many regions worldwide, such as the Gulfs of Tehuantepec, Papagayo, and Panama (Smith et al., 2015) the Columbia River Gorge (Sharp and Mass, 2004), and the straits and gaps in the Philippine Archipelago (Rypina et al., 2010). Several wind jets exist along the Red Sea region, covering both the Arabian Peninsula and the African continent. Jiang et al. (2009) observed a positive correlation between these jets and increases in air temperature. In the summer, from June to August, the Tokar Wind Jet is considered the most vital wind event compared to other wind jet events (Langodan et al., 2014, 2017; Pratt et al., 2020; Ralston et al., 2013).

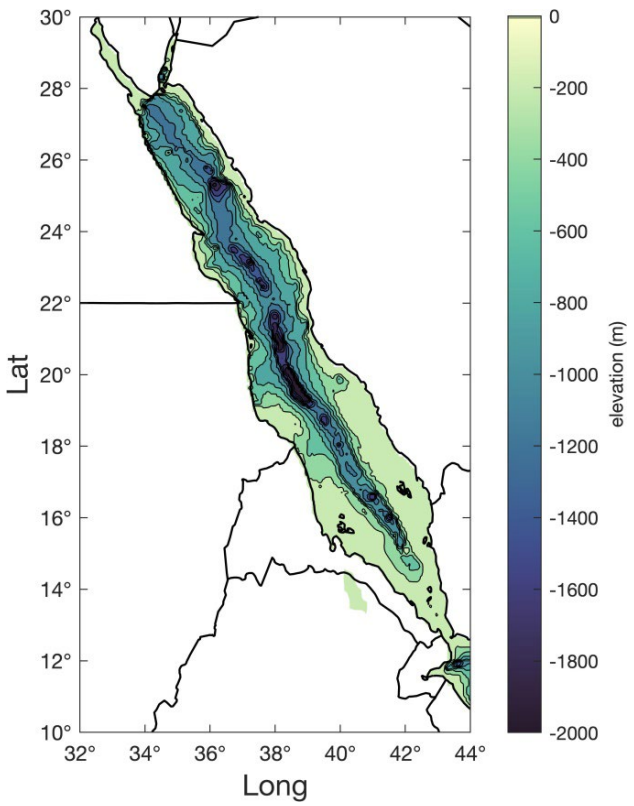

Figure 1. Map of the Red Sea basin and bathymetric features in meters [m] from the General Bathymetric Chart of the Oceans (GEBCO) datasets.

The Tokar Gap is one of the most significant gaps in the Red Sea's western coast: it has a 110 km width and is 50 km inland from the coast. Figure 2 shows the monthly mean SST over the Red Sea in conjunction with wind vectors during July and August. Wind jets from this gap can directly affect the surface winds above the Red Sea, which can reach 25 m/s^{-1} speeds (Pratt et al., 2020). In the summer, the wind jet blows from the Sahara Desert to the mountain gap, then into the Red Sea, driving dust storms into the basin, which are also considered one of the significant sources of silt in the northern hemisphere (Hickey and Goudie, 2007). This has an enhancement effect on the primary productivity in the area since it carries nutrients and mixes the water column. The strength of the wind changes the nutrient distribution in the basin by generating upwelled cold water, which is rich in nutrients (Smith et al., 2015). On the other hand, the wind jet system during winter reverses from the Red Sea to the mountain gap (Pedgley, 1974).

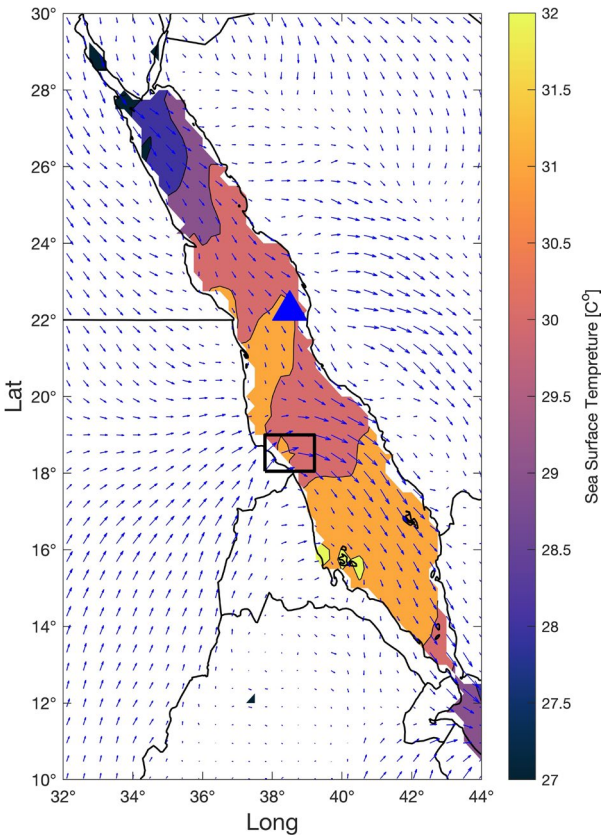

Figure 2. Monthly mean SST over the Red Sea (contour), with the mean wind (vectors) for July and August. The black box is the area of the Tokar Gap wind jet. The blue tringle is the Woods Hole Oceanographic Institution (WHOI) and King Abdullah University of Science and Technology (KAUST) buoy location.

In general, the SST is affected by several atmospheric factors, such as air temperature, evaporation, precipitation, and wind (Sultan and Ahmad, 1991). Moreover, ocean dynamics such as upwelling also play a major role in its variability. The area also experiences strong evaporation and nearly no precipitation, resulting in one of the most saline water basins in the world. Air temperature, wind, and evaporation have a direct impact on SST distribution in the northern part of the Red Sea, where it increases from north to south all year round (Morcos, 1970; Al-Subhi and Al-Aqsum, 2008). In the southern part of the Red Sea, SST is mainly influenced by monsoon-induced wind (Acker et al., 2008). According to Sofianos and Johns (2003), the highest SSTs are located at the center of the Red Sea and decrease both northward and southward. In addition, the eastern side of the Red Sea contains a higher SST than the western side of the Red Sea, and this difference can reach about two degrees at the same latitude (Morcos, 1970; Al-Subhi and Al-Aqsum, 2008; Taqi and Al-Subhi, 2012). Furthermore, Kim and Barros (2014) found that August has the warmest SST, whereas February has the coolest, and the difference in temperatures between them can reach 6°C (Berman et al., 2003).

It is well known that wind jets impact net heat flux components. These fluxes are represented by two radiation fluxes: shortwave (Q_s) and longwave radiation (Q_b), which mainly determine heat loss or gain by the sea. The shortwave radiation is the main energy source for the oceans and is represented by positive values, whereas the longwave radiation denotes the returned radiation to the atmosphere and is represented by negative values. Moreover, the other two turbulent fluxes are the latent heat flux (Q_e) and the sensible heat flux (Q_h). The latent heat

flux refers to the energy transferred from the sea to the atmosphere by evaporation; it is represented by negative values and is considered the main driving force for the atmosphere. The sensible heat flux refers to the energy that results from differences in air and sea temperatures. It can have either positive or negative values depending on the temperature differences. The study of heat flux is a critical element for understanding the interactions between the ocean and atmosphere, which are used for predicting climate and seasonal forecasts. Several studies on the subject of heat fluxes around the globe have been conducted (Li et al., 2011; Xiang-Hui and Fei, 2014; Hartmann, 2016; Kumar et al., 2017; Xiao et al., 2019; Eshghi et al., 2020). Moreover, flux studies have also been conducted in the Red Sea (Jiang et al., 2009; Papadopoulos et al., 2013; Zhai et al., 2015; Al Senafi et al., 2019; Nagy et al., 2021). Recently, there has been an increased emphasis on wind jets and their effects on the Red Sea. Primarily, a Weather Research and Forecasting (WRF) model with Advanced Research WRF (ARW) over a short period has been set up to study the cross-axis winds over the Red Sea (Jiang et al., 2009). In addition, Zhai and Bower (2013) examined sea level altimetry data located near the Tokar Gap and found that summer wind jets from the Tokar Gap form a cyclonic eddy in the north and an anticyclonic eddy in the south. This results in the generation of dipolar eddies, with a positive correlation between the dipolar and wind jet strength being found. This was also confirmed by Shanas et al. (2017), who also stated that, due to the Tokar Gap wind jets, the Red Sea can be separated into two parts, each with their own characteristics. Menezes et al. (2018) investigated the westward jets over the northern part of the Red Sea using ten-year wind data to determine the spatial and temporal variabilities of the jets and compare them with an *in situ* wind measurement. Their findings agreed with those of Bower and Farrar (2015), who found that westward winds result in intensive heat loss and evaporation over the northern Red Sea. Recently, Pratt et al. (2020) studied the dynamics and anatomy of the Tokar Wind Jet and the other two secondary jets by using Eulerian and Lagrangian analysis to quantify the energy from their pathways. Their findings showed that the Tokar Wind Jet is more powerful than the other two in terms of strength. This wind event could be one of the reasons for the extreme high and low events that occur during the summer season, as five extreme high events have been noted from 1985 to 2015 (Alawad et al., 2020).

As seen above, most of the previous studies have focused only on the dynamics of the Tokar Gap and its influence on the northern part of the Red Sea. In this study, however, more focus is given to the central part of the Red Sea. The main objective is to investigate the main factors that affect LHF in the central Red Sea near the Tokar Gap by using two decades of reanalysis data (2000-2020) and by applying EOF method.

The remaining parts of this study are as follows: Section 2 describes the datasets and methods used in this study. Section 3 and 4 presents the results and discussion, respectively. In addition, Section 5 features the conclusion.

METHODS

The atmospheric and oceanic data are from the reanalysis data centre ERA5 (Hersbach, 2016), which is the fifth generation of the European Centre for Medium-Range Weather Forecasts (ECMWF). This dataset covers the period from 1950 to the present and represents better atmospheric, land, and ocean reanalysis data compared to the previous reanalysis climate dataset. Furthermore, it has higher spatial and temporal resolutions, as well as improved accuracy in terms of wind stress and wind direction (Tetzner et al., 2019). The dataset can be downloaded from: https://www.ecmwf.int. The spatial resolution of ERA5 data is 0.25° x 0.25°, and the dataset has an hourly temporal resolution. Moreover, OAFlux was considered for validation purposes. WHOI's OAFlux is an ongoing global flux product with a spatial resolution of one degree. OAFlux combines satellite data with modelling and reanalysis data using an integrated analysis technique and COARE 3.0 to estimate heat fluxes (Jin and Willer, 2008). The OAFlux data is available at https://oaflux.whoi.edu/data-access/.

In this study, data from a period of almost 21 years (from 2000 to 2020) were used to study the influence of the eastward wind jet from the Tokar Gap on LHF over the central part of the Red Sea region between the latitudes 16° to 21° and longitudes 36° to 43°.

To validate the accuracy of ERA5 in the Red Sea, the data were tested using a surface buoy in the Red Sea located at (22.17°N; 38.50°E), as it is the only surface buoy in the Red Sea. The buoy mainly measured air temperature, humidity, SST, atmospheric pressure, short wave radiation, and long wave radiation. The COARE 3.0 algorithm (Fairall et al., 2003) has been used to estimate LHF and wind stress from the buoy measurements. In addition, LHF from OAFlux is used to validate ERA5 LHF values by following Wang et al. (2012). To compare observed and ERA5 data, the closest four grid points were interpolated bilinearly to the WHOI/KAUST buoy placed at (22.25°N 38°E), which was recently applied in the Red Sea by Al Senafi et al., (2019) and Zhou et al. (2018). Based on the occurrence time of the Tokar Wind Jet, which will be discussed further below, the July and August months from 2009 were selected for validation. Visualization and statistical parameters, such as correlation coefficient (CC), root mean square error (RMSE), and mean absolute differences (MAD) were considered to evaluate the ERA5 with the available observed data.

To achieve the aim of the study, the obtained data were cropped to solely comprise those from the summer period (June, July, August, and September), which is when the Tokar Wind Jet appears. After that, the data were filtered and cropped to the period when jet events are more pronounced. To calculate wind speed, the following formula was used:

$$W = \sqrt{u^2 + v^2} \quad (1)$$

Wind stress was calculated by the following formula:

$$\tau = \rho_a C_D W^2 \quad (2)$$

where ρ_a is the air density ≈ 1.2 kg/m^{-2}; C_D is the empirically determined drag coefficient ≈ 0.0013; and w is wind speed from equation (1). The hourly atmospheric data (wind stress, wind speed, LHF, SST) were processed to obtain the daily mean values by calculating the mean averaged hourly data. Since this study applied EOF, the LHF, SST, and wind speed data were converted into monthly averaged values from the mean averaged daily data. Quality control checks were applied on the time series of LHF, SST, wind speed, and wind stress to check for outliers and errors.

The empirical orthogonal functions (EOF) method, which was firstly applied by Lorenz (1956), is currently considered an effective applied technique for understanding temporal and spatial variabilities when studying atmospheric and oceanic science. The climate system is comprised of long-term statistical characteristics of atmospheric and oceanic conditions, resulting in a high degree of dimension. EOF assesses these variables by assembling the coherent variations of a collection of time series into several modes. Most of the differences are observed in the first two or three modes. EOF separates space and time fields into orthogonal spatial patterns referred to as empirical eigenvectors (EOF modes). These modes are coupled with eigenvalues that indicate the percentage of variance explained, and principal components (PCs) that describe how the amplitude of each EOF mode fluctuates over time (Björnsson, 1997). The generated new highest modes constitute a distinct phenomenon that can be statistically investigated using a variety of approaches such as correlation coefficients and the determination coefficient for the generated eigenvalues.

This method has been widely applied in several regions, such as the Red Sea region (Alawad et al., 2020; Menezes et al., 2018; Mohamed et al., 2021; Abdulla and Al-Subhi, 2020; Alawad et al., 2019), the Arabian Gulf region (Al-Subhi & Abdulla, 2021; Siddig et al., 2021), in the Amazon basin (Villar et al., 2009), in northwest Mexico (Gochis et al., 2006), and in the Southern Great Plains (Kim and Barros, 2002). In this study, the monthly averaged data were used to enhance the EOF modes of variety by almost three times in comparison with the daily values (Feldstein, 2000). Furthermore, to investigate the effective spatial modes of variability, the EOF function applied in this study was based on the climate data toolbox by Greene et al. (2019). The EOF formula is expressed as:

$$Z(x, y, t) = \sum_{k=1}^{N} (PC(t) \times EOF(x, y)) \quad (3)$$

where $Z(x, y, t)$ is the original time series as it relates to time (t) and space (x, y), $PC(t)$ is the principal component that is responsible for how the effectiveness of each EOF changes over time, and EOF (x, y) represents the spatial structures

(x, y) of the key factors that can influence the temporal variations in Z.

The coefficient of determination (R^2) was also applied to investigate the relationship between the parameters. The formula is expressed as:

$$R^2 = \left(\frac{n\,\Sigma(xy) - (\Sigma x)(\Sigma y)}{\sqrt{n(\Sigma x^2) - (\Sigma x)^2}\,\sqrt{n(\Sigma y^2) - (\Sigma y)^2}}\right)^2 \quad (4)$$

where n is the number of variables and x, y represent the means of the independent and dependent variables of the regression, respectively.

On the other hand, partial correlation is also applied to measure the relationship between two variables with the effect of a controlling variable removed. Partial correlation between x, y with the removed effect of Z is expressed as:

$$r_{XY|Z} = \frac{(r_{XY} - r_{XZ}r_{YZ})}{\sqrt{(1 - r_{XZ}^2)(1 - r_{YZ}^2)}}$$

RESULTS

Positive signs in LHF represent heat gain, and minus signs indicate that the water is evaporating. In this study, all LHF are represented by positive signs since this study does not focus on the other heat flux components. Figure 3 shows a time series for the chosen period of July and August from 2009, which contains air temperature, SST, LHF, and wind stress for the observed data from the buoy and the ERA5 data with the estimated LHF and wind stress from COARE 3.0 using ERA5 parameters.

It is clear from Figures 3a and 3b that the time series of air temperature and SST had similar patterns. For both parameters, the temperature ranged from 30° to 33°C for all periods. While the time series in Figure 3c fluctuated, the overall trend was the same. Figure 3d presents a comparison of LHF values from ERA5, observed data, and OAFlux.

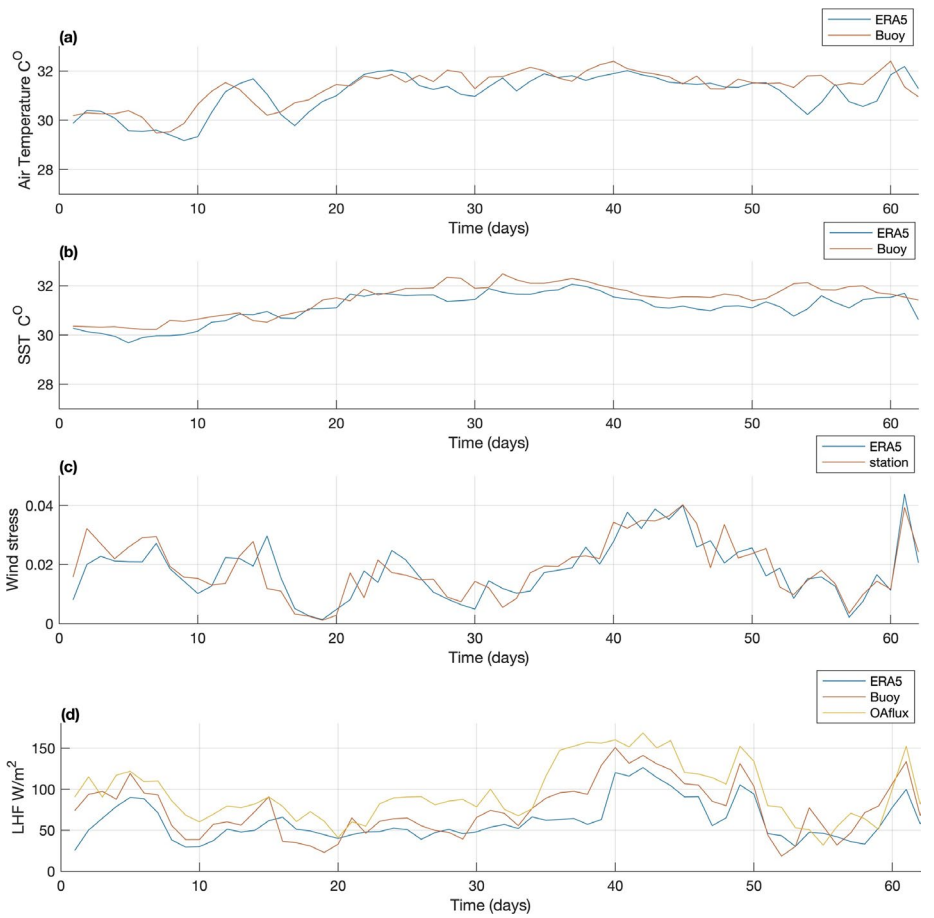

Figure 3. Daily mean time series of (a) Air temperature, (b) SST, (c) wind stress and (d) HF for the period of July – Augustfor 2009.

Table 1 presents the statistical results of the time series of ERA5 data in Figure 3. Following the correlation coefficients, the two data sets are highly correlated. The RMSE for air temperature, SST, LHF, and wind stress are 0.558, 0.451, 22.770, and 0.005, respectively. Furthermore, the MAD values are also acceptable for all the tested parameters. In terms of the OAFlux data, the statistical results also demonstrated similar values to the observed and ERA5 data.

Figure 4 illustrates the spatial monthly mean SST and wind speed vectors for the central part of the Red Sea. As can be seen, the strong cross wind vectors from the African coast, which are the Tokar Wind Jets, are located in a box near the Wind Jet entrance.

Table 1. Summary of the statistical analysis between ERA5 and observed data for Air temperature, SST, LHF and wind stress. On the right side, statistical analysis between OAFlux and observed for LHF.

	ERA5			OAFlux		
Parameters	CC	RMSE	MAD	CC	RMSE	MAD
Air temperature (℃)	0.78	0.558	0.431	-	-	-
SST (℃)	0.87	0.451	0.354	-	-	-
Wind stress (N/m^2)	0.83	0.005	0.004	-	-	-
LHF (W/m^2)	0.85	22.770	19.77	0.849	27.39	23.57

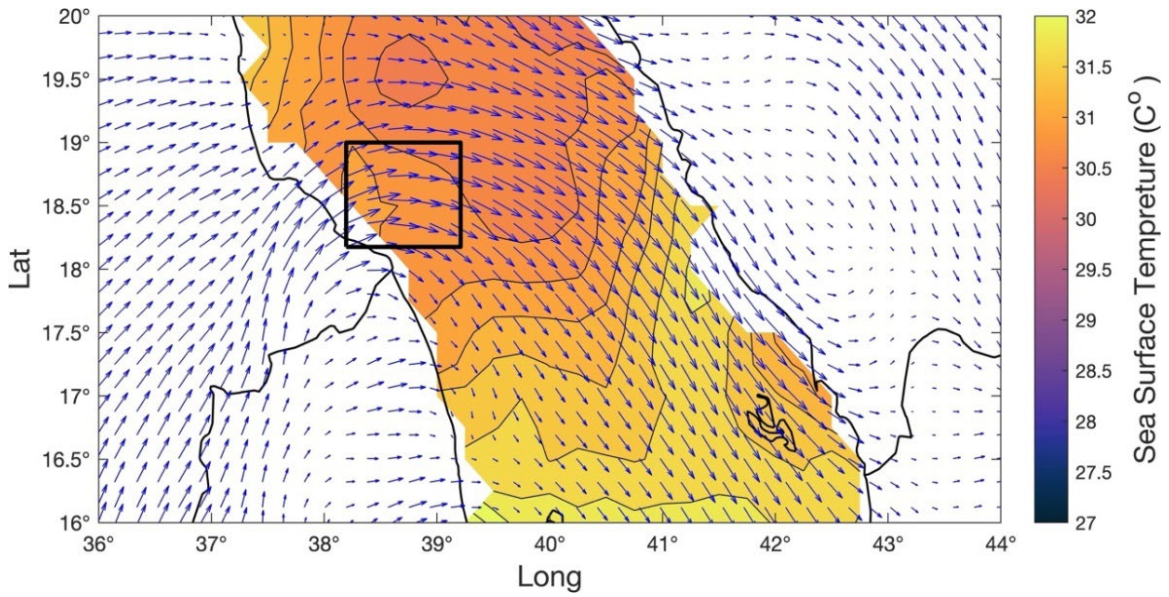

Figure 4. Monthly mean SST (contour) and wind speed (vectors) in central Red Sea for summer; the black box contains the highest wind vectors from Tokar Gap.

In addition, to identify the occurrence time of such events, a three-year period from 2011 to 2013 for the daily time series of the LHF, wind speed, and SST parameters during the summer months (June, July, August, and September) was considered (Figure 5).

As the data show, jet events were more pronounced during July and August; thus, June and September were discarded from the analysis. Figure 6 shows the daily mean time series for July and August from 2000 to 2020 for the LHF, wind speed, and SST.

Figure 5. Daily mean time series of (a) LHF, (b) wind speed and (c) SST (d) humidity during summer months (June, July, August and September) from 2011-2013.

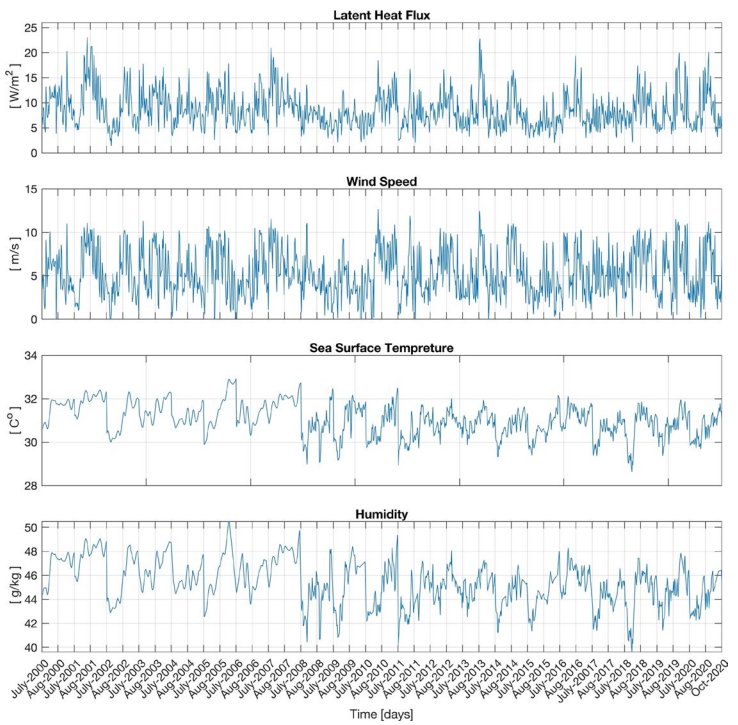

Figure 6. Daily mean time series of (a) LHF, (b) wind speed, (c) SST and (d) humidity for the entire period (2000-2020).

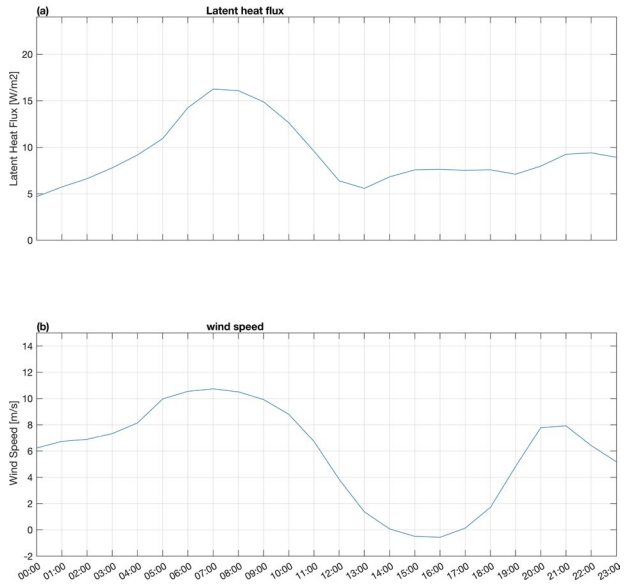

Figure 7. Diurnal variability for (a) LHF and (b) wind speed.

Figure 7 illustrates the daily variations of LHF and wind speed near the Tokar Gap. Wind speed and LHF instantly increased at 00:00, peaked in the early morning, and then dropped to reach their minimum values between 14:00 and 18:00.

For further analysis, Table 2 represents the mean and maximum values of the daily time series. The maximum daily value of LHF was determined to be about 22.99 w/m^{-2} , and the maximum value of SST reached 32.91°C. On the other hand, the maximum and mean daily values for wind speed were 13.84 m/s^{-2} and 7.32 m/s^{-2}, respectively. In addition, the daily mean values for LHF and SST were 8.58 w/m^{-2} and 31.05°C, respectively.

Table 2.: Summary of the statistical analysis for the daily averaged time series of LHF, wind speed and SST for the entire period (2000-2020).

	Max	Mean
LHF (w/m^{-2})	22.99	8.58
Wind speed (m/s^{-2})	13.84	7.32
SST (°C)	32.91	31.05

Table 3 shows wind speed events faster than 12 m/s^{-2} from the daily mean time series. A total of 12 wind events with an average speed of 12.72 m/s^{-2} were recorded, with the highest speed recorded on the 24th of July 2010, when the wind speed peaked at 13.84 m/s^{-2}

Table 3. Summary of the eastward wind jets from Tokar Gap higher than 12 m/s from the daily averaged mean data.

Number of events	Date of events	Wind jet speed (m/s^{-2})
1	17-Aug-2000	12.20
2	26-Jul-2001	12.76
3	09-Jul-2003	12.52
4	05-Jul-2007	12.95
5	24-Jul-2010	13.84
6	24-Jul-2011	13.15
7	01-Au g-2013	13.52
8	31-Aug-2014	12.18
9	05-Aug-2019	12.80
10	10-Aug-2019	12.42
11	23-Aug-2019	12.27
12	06-Aug-2020	12.49

Figure 8 illustrates the monthly averaged time series of LHF versus wind stress. The two parameters demonstrated a strong relationship, as if the wind stress led to a corresponding increase in LHF. Statistically, the parameters showed a significant 0.83 correlation.

This study used the EOF method to define the LHF mode of variability. Table 4 lists the highest modes generated by the EOF. The leading first two modes represented about ~90.8% of the variability. The first mode contributed 80.9%, whereas the second mode contributed 9.9%. The last four modes contributions ranged from 0.8% to 2.1%, which showed that they are relatively small compared to the first two modes.

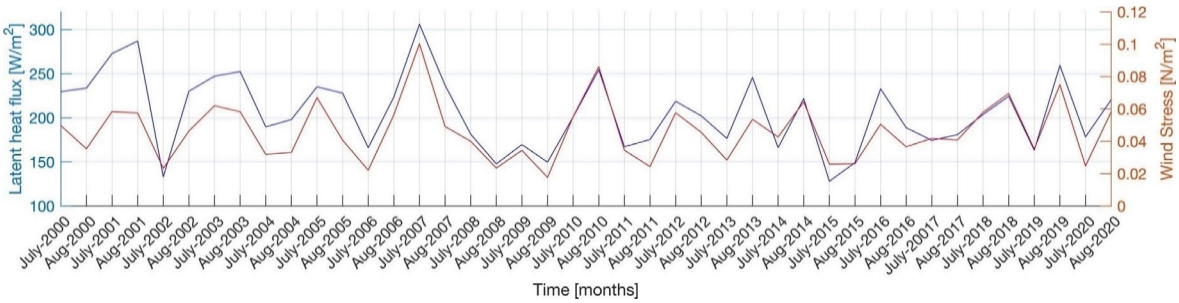

Figure 8. Monthly averaged time series of LHF and wind stress for the entire period (2000-2020).

Table 4. Summary of the first six modes of viability generated by the EOF.

Modes	Modes of variability	Cumulative variance
Mode 1	80.9%	80.9
Mode 2	9.9%	90.8
Mode 3	2.1%	92.9
Mode 4	1.7%	94.6
Mode 5	0.1%	94.7
Mode 6	0.8%	95.5

Figure 9 illustrates the spatial distribution of the first two modes. The highest variability is near The Tokar Gap is located between the latitudes of 18.5°N and 19°N and the longitudes of 38.2°E and 38.8°E (Figure 9a).On the other hand, the spatial distribution of this mode seemed to be homogeneous, except that there were different values located on the Red Sea's eastern coast (Figure 9b).

The principal components of EOF are illustrated in Figure 10. The results showed a sharp fluctuation behavior for PC1, while PC2 did not show as much fluctuation. Interestingly, both principal components had the same pattern. In the first decade, 2000-2010, most variabilities amplitudes were in positive signs, while the opposite was in the last decade.

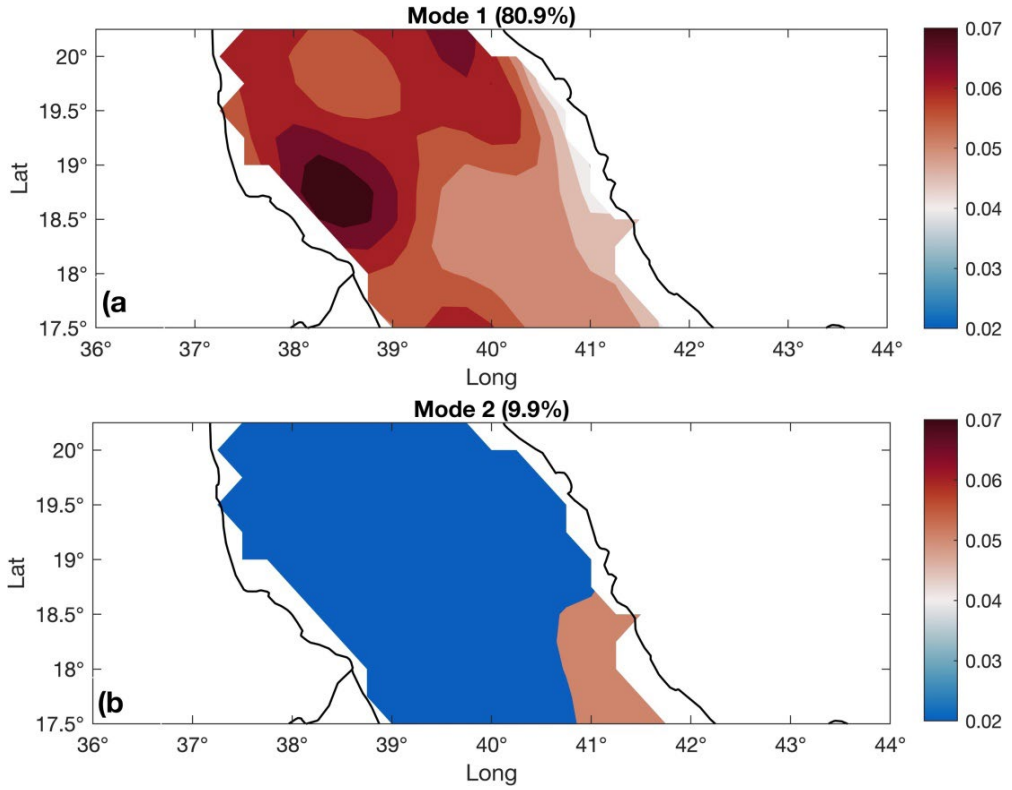

Figure 9. Spatial patterns of the first two EOF modes of LHF.

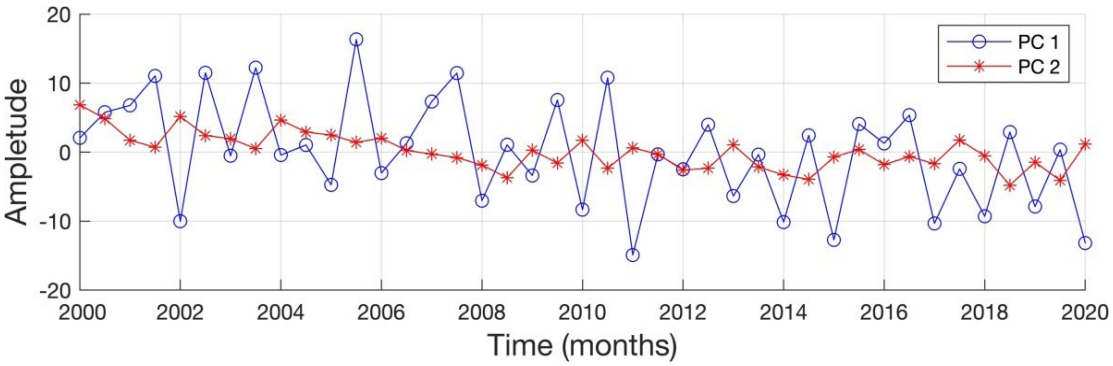

Figure 10. Time series of the first two principal components corresponding to the EOF modes.

The mean value of the highest wind jets near the Tokar Gap entrance is presented in Figure 4. In Table 5, the correlation and determination coefficient are applied to SST and wind speed for the located point with PC1 and PC2. The first examined factor was SST, which showed a high correlation coefficient with PC1 by 0.90 and a determination coefficient (DC) of 81.99%. The second investigation was of wind speed with PC1 and PC2. The result showed a positive correlation between wind speed and PC1 by 0.35 and a DC of 12.80%. Partial correlation results between SST and wind speed with LHF variability showed a good correlation of 0.68.

Table 5. Summary of the correlation coefficient, P-values and determination coefficient values of the first two principal components (PC1 and PC2) with SST and wind stress.

Variability	PC1			PC2		
	CC (%)	P-value	DC (%)	CC (%)	P-value	DC (%)
SST	0.90	0.00	81.99	0.20	0.02	4.09
Wind stress	0.35	0.01	12.8	0.17	0.09	2.88

DISCUSSION

The present study is designed to investigate the influence of atmospheric and oceanic factors near the Tokar Gap on LHF using the EOF method. Initially, validating reanalysis data with observed data is crucial to test the accuracy of the ERA5 data. According to the validation analysis results in Figure 3 and Table 1, ERA5 is generally in agreement with the observed data. This confirms the validity of the data in the Red Sea, which is consistent with several studies (Al Senafi et al., 2019; Bower and Farrar, 2015; Aboobacker et al., 2020; Bawadekji et al., 2022).

Following the method that Zhai and Bower (2013) applied, the mean sum of the highest wind vectors in the box in Figure 4 was used to calculate the offshore daily winds near the Tokar Gap. The mean sum of SST, LHF, wind speed, and wind stress from this calculation method were used for further analysis.

The result of identifying the most pronounced events showed that July and August contain more and higher wind jets, as shown in Figure 5. These event periods are consistent with several previous studies (Jiang et al., 2009; Zhai & Bower, 2013; Nicholls et al., 2015), which used different methods to present wind jets.

The Tokar Gap have a diurnal influence on LHF, as shown in Figure 7. LHF and wind speed had nearly the same pattern since they start rising at 00:00 and reach their peak between 05:00 to 06:00. These patterns are consistent with several previous studies in the Red Sea region (Jiang et al., 2009; Davis et al., 2015; Pratt et al., 2020). According to Jiang et al., (2009), the Tokar Wind Jet has a strong diurnal fluctuation due to the significant cross-shore temperature differential during the day, which results in westward sea winds during the day and eastward land breezes during the night. In the summer, the Tokar Wind Jet is, thus, stronger in the early morning than in the evening.

In Figure 8, the LHF and wind speed seemed to have a strong relationship, which agrees with the findings of several previous studies (Jiang et al., 2009; Davis et al., 2015; Feng et al., 2021).

The EOF spatial and temporal patterns of LHF in the central Red Sea are shown in Figures 9 and 10, respectively. The highest first mode spatial distribution results are in line with the spatial pattern of Mohamed et al. (2021a), who used monthly averaged SST data and found that the central and southern parts of the Red Sea contain the highest variability in their first mode, standing at about 51.65%.

As a result of its small contribution, the second mode showed few differences in its spatial pattern.

In terms of the temporal patterns, PC1 and PC2, the first two principal components, showed a high difference in their variability. As shown in Figure 9, the PC trends indicate that the LHF rates have been increasing in the last ten years between 2010 and 2020. This increase of LHF may be related to the increased SST, as shown by (Alawad et al., 2020; Mohamed et al., 2021a).

Kumar et al., (2017) also found that LHF increases with SSTs in warm basins with temperatures higher than 25°C. Their findings may be a key factor for affected LHF rates in the Red Sea.

Previous studies have attempted to explore LHF sensitivity to SST and wind speed (Li et al., 2011; Xiang-Hui and Fei, 2014; Hartmann, 2016; Kumar et al., 2017; Eshghi et al., 2020). These studies indicate that LHF is sensitive to SST and wind speed change. To test their sensitivity, the mean value from the located box in Figure 4 is used to investigate the contributions of SST and wind speed to the first two principal components by applying the correlation and the determination coefficients. Based on the statistical analysis of SST with PC1, the results agree with the long-term results of Xiao et al. (2019), who found that SST contributed with 84.3% to the South China Sea's first mode. In addition, PC2 had a smaller CC than PC1, whose DC was 4.09%. Furthermore, the other investigation was on wind speed with both PC. This investigation's results were relatively small compared to those recorded by previous studies (Eshghi et al., 2020; Xiang-Hui and Fei, 2014), which studied wind speed variability and obtained high explained variances of 95% and 91.50%, respectively. Therefore, our current results do not show an agreement with their results. Furthermore, the former experiment studied the Pacific region for nearly three decades, while the latter studied the Arabian Sea for about two decades. As evidenced by our results, the study size and period might affect the EOF results.

This analysis shows that PC1 was related to SST while PC2 was related to wind speed, which might indicate that SST has a higher contribution to LHF than wind speed based on the EOF method. Therefore, SST could play a major role in controlling LHF rates in the study region.

The minimal contribution of wind speed to LHF may be due to the strong link between SST and the specific humidity differences of saturation and actual vapor pressure, as observed in Figures 5 and 6. According to the study of Eshel and Naik (1997), significant fluctuations in specific humidity with high relative SST values might slightly improve LHF verbality.

Moreover, the partial correlation results between SST and wind speed and LHF results indicate that SST and wind speed with LHF have a partial correlation of 0.68. Based on this study, SST showed a direct relation to LHF variability, while the wind speed showed an indirect relation LHF. This relation can be related to the results by Wang et al (1998.) that showed that wind speed, LHF, and SST are interacted by each other by both direct and indirect ways.

CONCLUSION

The current study was conducted using atmospheric and oceanic reanalysis data from ERA5 covering the period between 2000 and 2020 for the central part of the Red Sea. In this investigation, the aim was to determine the effects of wind jets from the Tokar Gap on the LHF at the central part of the Red Sea by applying the EOF method. Wind jet events were found to be more pronounced during July and August. The maximum daily values of LHF, SST, and wind speed were 22.99 w/m^{-2}, 32.91°C, and 13.84 m/s^{-2}, respectively. The diurnal variability on LHF in Tokar Gap during the summer was stronger in the early morning than in the evening, when maximum and

minimum values for LHF were 16.24 w/m^{-2} and 5.57 w/m^{-2}, respectively.

The results of this study showed that there was a significant correlation between wind stress and LHF at about 0.83%. The results of the EOF analysis indicated that the first two modes represented around 90.8%. To be more precise, the first mode showed a variability of 80.9%, and the highest explained variance was located near the Tokar Wind Jet entrance, while the second mode seemed to be homogeneous, with about 9.9% variability found in most study areas. The correlation coefficient and determination coefficient were applied on the time series of PC1 with SST and wind speed. These results indicated that PC1 was positively correlated with SST by 0.90 and a DC of 81.99%. In addition, PC1 with wind speed showed a CC of 0.35 and a DC of 12.80%. This analysis reveals that SST had the most substantial influence on LHF viability near the Tokar Gap.

ACKNOWLEDGMENTS

The authors would like to thank the Copernicus Climate Change Service Information for generating and providing ERA5 data. Additionally, we thank Woods Hole Oceanographic Institution (WHOI) and King Abdullah University of Science and Technology (KAUST) for providing mooring data. We also thank the reviewers for their comments and suggestions, which improved our work.

AUTHOR CONTRIBUTIONS

J.A.T: Conceptualization, Data curation, formal analysis, investigation, methodology, resources, writing original draft, software.

A.M.S: Guidance, methodology, supervision, writing-review & editing. Data curation, validation, visualization.

F.A.M: Guidance, methodology, supervision, writing-review & editing. Data curation, software, validation, visualization.

REFERENCES

Abdulla, C. & Al-Subhi, A. 2020. Sea Level Variability in the Red Sea: A Persistent East–West Pattern. *Remote Sensing*, *12*(13), 2090. DOI: https://doi.org/10.3390/rs12132090

Aboobacker, V. M., Shanas, P. R., Al-Ansari, E. M. A. S., Kumar, V. S. & Vethamony, P. 2020. The maxima in northerly wind speeds and wave heights over the Arabian Sea, the Arabian/Persian Gulf and the Red Sea derived from 40 years of ERA5 data. *Climate Dynamics*, *56*(3–4), 1037–1052. DOI: https://doi.org/10.1007/s00382-020-05518-6

Acker, J., Leptoukh, G., Shen, S., Zhu, T. & Kempler, S. 2008. Remotely-sensed chlorophyll a observations of the northern Red Sea indicate seasonal variability and influence of coastal reefs. *Journal of Marine Systems*, *69*(3–4), 191–204. DOI: https://doi.org/10.1016/j.jmarsys.2005.12.006

Alawad, K. A., Al-Subhi, A. M., Alsaafani, M. A. & Alraddadi, T. M. 2020. Decadal variability and recent summer warming amplification of the sea surface temperature in the Red Sea. *PLOS ONE*, *15*(9), e0237436. DOI: https://doi.org/10.1371/journal.pone.0237436

Alawad, K. A., Al-Subhi, A. M., Alsaafani, M. A., Alraddadi, T. M., Ionita, M. & Lohmann, G. 2019. Large-Scale Mode Impacts on the Sea Level over the Red Sea and Gulf of Aden. *Remote Sensing*, *11*(19), 2224. DOI: https://doi.org/10.3390/rs11192224

Al-Subhi, A. & Al-Aqsum, M. M. 2008. Temporal and Spatial Variations of Remotely Sensed Sea Surface Temperature in the Northern Red Sea. *Journal of King Abdulaziz University, Marine Science*, *19*, 61–74.

Al-Subhi, A. M. & Abdulla, C. P. 2021. Sea-Level Variability in the Arabian Gulf in Comparison with Global Oceans. *Remote Sensing*, *13*(22), 4524. DOI: https://doi.org/10.3390/rs13224524

Bawadekji, A., Tonbol, K., Ghazouani, N., Becheikh, N. & Shaltout, M. 2022. Recent atmospheric changes and future projections along the Saudi Arabian Red Sea Coast. *Scientific Reports*, *12*(1). DOI: https://doi.org/10.1038/s41598-021-04200-z

Berman, T., Paldor, N. & Brenner, S. 2003. Annual SST cycle in the Eastern Mediterranean, Red Sea and Gulf of Elat. *Geophysical Research Letters*, *30*(5), n/a-n/a. DOI: https://doi.org/10.1029/2002gl015860

Björnsson, H., & Venegas, S. A. (1997). A manual for EOF and SVD analyses of climatic data. *CCGCR Report*, 97(1), 112-134.

Bower, A. S. & Farrar, J. T. 2015. Air–Sea Interaction and Horizontal Circulation in the Red Sea. *In*: *The Red Sea* (pp. 329–342). Springer Berlin Heidelberg. DOI: https://doi.org/10.1007/978-3-662-45201-1_19

Davis, S. R., Pratt, L. J. & Jiang, H. 2015. The Tokar Gap Jet: Regional Circulation, Diurnal Variability, and Moisture Transport Based on Numerical Simulations. *Journal of Climate*, *28*(15), 5885–5907. DOI: https://doi.org/10.1175/jcli-d-14-00635.1

Eshel, G. & Naik, N. H. 1997. Climatological Coastal Jet Collision, Intermediate Water Formation, and the General Circulation of the Red Sea. *Journal of Physical Oceanography*, *27*(7), 1233–1257. DOI: https://doi.org/10.1175/1520-0485(1997)027<1233:CCJCIW>2.0.CO;2

Eshghi, N., Barzandeh, A., Hosseinibalam, F. & Hassanzadeh, S. 2020. Investigating dynamic and static aspects of regional sea level changes in the north-western Indian Ocean. *Bulletin of Geophysics and Oceanography*, *61*(2), 249–270.

Fairall, C. W., Bradley, E. F., Hare, J. E., Grachev, A. A. & Edson, J. B. 2003. Bulk Parameterization of

Air–Sea Fluxes: Updates and Verification for the COARE Algorithm. *Journal of Climate*, *16*(4), 571–591. DOI: https://doi.org/10.1175/1520-0442(2003)016<0571:BPOASF>2.0.CO;2

Feng, X., Sun, J., Yang, D., Yin, B., Gao, G. & Wan, W. 2021. Effect of Drag Coefficient Parameterizations on Air–Sea Coupled Simulations: A Case Study for Typhoons Haima and Nida in 2016. *Journal of Atmospheric and Oceanic Technology*, *38*(5), 977–993. DOI: https://doi.org/10.1175/jtech-d-20-0133.1

Gochis, D. J., Brito-Castillo, L. & Shuttleworth, W. J. 2006. Hydroclimatology of the North American Monsoon region in northwest Mexico. *Journal of Hydrology*, *316*(1–4), 53–70. DOI: https://doi.org/10.1016/j.jhydrol.2005.04.021

Hartmann, D. L. 2016. The Energy Balance of the Surface. *In*: *Global Physical Climatology* (pp. 95–130). Elsevier. DOI: https://doi.org/10.1016/b978-0-12-328531-7.00004-9

Hersbach, H. 2016. The ERA5 Atmospheric Reanalysis (pp. NG33D-01). Presented at the AGU fall meeting, New Orleans: AGU.

Hickey, B. & Goudie, A. S. 2007. The use of TOMS and MODIS to identify dust storm sourceareas : the Tokar Delta (Sudan) and the Seistan Basin (south west Asia). *Geomorphological Variations*, 37–57.

Jiang, H., Farrar, J. T., Beardsley, R. C., Chen, R. & Chen, C. 2009. Zonal surface wind jets across the Red Sea due to mountain gap forcing along both sides of the Red Sea. *Geophysical Research Letters*, *36*(19). DOI: https://doi.org/10.1029/2009gl040008

Jin, X. & Weller, R. A. 2008. *Multidecade global flux datasets from the objectively analyzed air-sea fluxes(oaflux) project: Latent and sensible heat fluxes, ocean evaporation, and related surfacemeteorological variables lisan yu. OAFlux*. Barnstable Town: Woods Hole Oceanographic Institution.

Kim, G. & Barros, A. P. 2002. Space–time characterization of soil moisture from passive microwave remotely sensed imagery and ancillary data. *Remote Sensing of Environment*, *81*(2–3), 393–403. DOI: https://doi.org/10.1016/s0034-4257(02)00014-7

Kumar, B. P., Cronin, M. F., Joseph, S., Ravichandran, M. & Sureshkumar, N. 2017. Latent Heat Flux Sensitivity to Sea Surface Temperature: Regional Perspectives. *Journal of Climate*, *30*(1), 129–143. DOI: https://doi.org/10.1175/jcli-d-16-0285.1

Langodan, S., Cavaleri, L., Vishwanadhapalli, Y., Pomaro, A., Bertotti, L. & Hoteit, I. 2017. The climatology of the Red Sea - part 1: the wind. *International Journal of Climatology*, *37*(13), 4509–4517. DOI: https://doi.org/10.1002/joc.5103

Langodan, S., Cavaleri, L., Viswanadhapalli, Y. & Hoteit, I. 2014. The Red Sea: A Natural Laboratory for Wind and Wave Modeling. *Journal of Physical Oceanography*, *44*(12), 3139–3159. DOI: https://doi.org/10.1175/jpo-d-13-0242.1

Li, G., Ren, B., Yang, C. & Zheng, J. 2011. Revisiting the trend of the tropical and subtropical Pacific surface latent heat flux during 1977–2006. *Journal of Geophysical Research*, *116*(D10). DOI: https://doi.org/10.1029/2010jd015444

Lorenz, E. N. 1956. *Empirical orthogonal functions and statistical weather prediction* (Vol. 1). Cambridge: Massachusetts Institute of Technology.

Menezes, V. V., Farrar, J. T. & Bower, A. S. 2018. Westward mountain-gap wind jets of the northern Red Sea as seen by QuikSCAT. *Remote Sensing of Environment*, *209*, 677–699. DOI: https://doi.org/10.1016/j.rse.2018.02.075

Mohamed, B., Nagy, H. & Ibrahim, O. 2021a. Spatiotemporal Variability and Trends of Marine Heat Waves in the Red Sea over 38 Years. *Journal of Marine Science and Engineering*, *9*(8), 842. DOI: https://doi.org/10.3390/jmse9080842

Morcos, S. A. 1970. Physical and chemical oceanography of the Red Sea. *In*: *Oceanography and Marine Biology, Annual Review* (Vol. 8, pp. 73–202).

Nagy, H., Mohamed, B., & Ibrahim, O. 2021. Variability of Heat and Water Fluxes in the Red Sea Using ERA5 Data (1981–2020). *Journal of Marine Science and Engineering*, 9(11), 1276. DOI: https://doi.org/10.3390/jmse9111276.

Nicholls, J. F., Toumi, R. & Stenchikov, G. 2015. Effects of unsteady mountain-gap winds on eddies in the Red Sea. *Atmospheric Science Letters*, 16(3), 279–284 DOI: https://doi.org/10.1002/asl2.554

Papadopoulos, V. P., Abualnaja, Y., Josey, S. A., Bower, A., Raitsos, D. E., Kontoyiannis, H. & Hoteit, I. 2013. Atmospheric Forcing of the Winter Air–Sea Heat Fluxes over the Northern Red Sea. *Journal of Climate*, *26*(5), 1685–1701. DOI: https://doi.org/10.1175/jcli-d-12-00267.1

Patzert, W. C. 1974. Wind-induced reversal in Red Sea circulation. *Deep Sea Research and Oceanographic Abstracts*, *21*(2), 109–121. DOI: https://doi.org/10.1016/0011-7471(74)90068-0

Pratt, L. J., Albright, E. J., Rypina, I. & Jiang, H. 2020. Eulerian and Lagrangian Comparison of Wind Jets in the Tokar Gap Region. *Fluids*, *5*(4), 193. DOI: https://doi.org/10.3390/fluids5040193

Ralston, D. K., Jiang, H. & Farrar, J. T. 2013. Waves in the Red Sea: Response to monsoonal and mountain gap winds. *Continental Shelf Research*, *65*, 1–13. DOI: https://doi.org/10.1016/j.csr.2013.05.017

Reed, T. R. 1931. Gap winds of the strait of Juan de Fuca. *Monthly Weather Review*, *59*(10), 373–376.

Rypina, I. I., Pratt, L. J., Pullen, J., Levin, J. & Gordon, A. L. 2010. Chaotic Advection in an Archipelago\ast. *Journal of Physical Oceanography*, *40*(9), 1988–2006. DOI: https://doi.org/10.1175/2010jpo4336.1

Senafi, F. A., Anis, A. & Menezes, V. 2019. Surface Heat Fluxes over the Northern Arabian Gulf and the Northern Red Sea: Evaluation of ECMWF-ERA5 and NASA-MERRA2 Reanalyses. *Atmosphere*, *10*(9), 504. DOI: https://doi.org/10.3390/atmos10090504

Shanas, P. R., Aboobacker, V. M., Albarakati, A. 167emM A. & Zubier, K. 167emM. 2017. Climate driven variability of wind-waves in the Red Sea. *Ocean Modelling*, *119*, 105–117. DOI: https://doi.org/10.1016/j.ocemod.2017.10.001

Sharp, J. & Mass, C. F. 2004. Columbia Gorge Gap Winds: Their Climatological Influence and Synoptic Evolution. *Weather and Forecasting*, *19*(6), 970–992. DOI: https://doi.org/10.1175/826.1

Siddig, N. A., Al-Subhi, A. M., Alsaafani, M. A. & Alraddadi, T. M. 2021. Applying Empirical Orthogonal Function and Determination Coefficient Methods for Determining Major Contributing Factors of Satellite Sea Level

Anomalies Variability in the Arabian Gulf. *Arabian Journal for Science and Engineering*, *47*(1), 619–628. DOI: https://doi.org/10.1007/s13369-021-05612-9

Smith, D. K., Li, X., Keiser, K. & Flynn, S. 2014. Regional Air-Sea interactions (RASI) climatology for central america coastal gap wind and upwelling events. *In*: *2014 Oceans - St. John's*. IEEE. DOI: https://doi.org/10.1109/oceans.2014.7003127

Sofianos, S. S. 2003. An Oceanic General Circulation Model (OGCM) investigation of the Red Sea circulation: 2. Three-dimensional circulation in the Red Sea. *Journal of Geophysical Research*, *108*(C3). DOI: https://doi.org/10.1029/2001jc001185

Taqi, A., & Al-Subhi, A. M. 2012. *Temporal and Spatial Patterns of Remotely Sensed Sea Surface Temperature in The Southern Red Sea*. DOI: https://doi.org/10.13140/RG.2.2.28487.80801

Tetzner, D., Thomas, E. & Allen, C. 2019. A Validation of ERA5 Reanalysis Data in the Southern Antarctic Peninsula—Ellsworth Land Region, and Its Implications for Ice Core Studies. *Geosciences*, *9*(7), 289. DOI: https://doi.org/10.3390/geosciences9070289

Villar, J. C. E., Ronchail, J., Guyot, J. L., Cochonneau, G., Naziano, F., Lavado, W., Oliveira, E. D., Pombosa, R. & Vauchel, P. 2009. Spatio-temporal rainfall variability in the Amazon basin countries (Brazil, Peru, Bolivia, Colombia, and Ecuador). *International Journal of Climatology*, *29*(11), 1574–1594. DOI: https://doi.org/10.1002/joc.1791

Wang, D., Zeng, L., Xixi Li & Shi, P. 2013. Validation of Satellite-Derived Daily Latent Heat Flux over the South China Sea, Compared with Observations and Five Products. *Journal of Atmospheric and Oceanic Technology*, *30*(8), 1820–1832. DOI: https://doi.org/10.1175/JTECH-D-12-00153.1

Xiang-Hui, F. & Fei, Z. 2014. Effect of Decadal Changes in Air-Sea Interaction on the Climate Mean State over the Tropical Pacific. *Atmospheric and Oceanic Science Letters*, *7*(5), 400–405. DOI: https://doi.org/10.1080/16742834.2014.11447197

Xiao, F., Wang, D., Zeng, L., Liu, Q.-Y. & Zhou, W. 2019. Contrasting changes in the sea surface temperature and upper ocean heat content in the South China Sea during recent decades. *Climate Dynamics*, *53*(3–4), 1597–1612. DOI: https://doi.org/10.1007/s00382-019-04697-1

Zhai, P. & Bower, A. 2013. The response of the Red Sea to a strong wind jet near the Tokar Gap in summer. *Journal of Geophysical Research: Oceans*, *118*(1), 421–434. DOI: https://doi.org/10.1029/2012jc008444

Zhai, P., Pratt, L. J. & Bower, A. 2015. On the Crossover of Boundary Currents in an Idealized Model of the Red Sea. *Journal of Physical Oceanography*, *45*(5), 1410–1425. DOI: https://doi.org/10.1175/jpo-d-14-0192.1

Zhou, F., Zhang, R., Shi, R., Chen, J., He, Y., Wang, D. & Xie, Q. 2018. Evaluation of OAFlux datasets based on in situ air–sea flux tower observations over Yongxing Island in 2016. *Atmospheric Measurement Techniques*, *11*(11), 6091–6106. DOI: https://doi.org/10.5194/amt-11-6091-2018